A Modular Design Framework for the Systematic Development of Primitive, Application-Specific Optical Modulation Tools

Nathan Tessema Ersumo

Electrical Engineering and Computer Sciences
University of California at Berkeley

Technical Report No. UCB/EECS-2020-180
http://www2.eecs.berkeley.edu/Pubs/TechRpts/2020/EECS-2020-180.html

September 16, 2020

Copyright © 2020, by the author(s).
All rights reserved.

Permission to make digital or hard copies of all or part of this work for personal or classroom use is granted without fee provided that copies are not made or distributed for profit or commercial advantage and that copies bear this notice and the full citation on the first page. To copy otherwise, to republish, to post on servers or to redistribute to lists, requires prior specific permission.

A Modular Design Framework for the Systematic Development of Primitive, Application-Specific Optical Modulation Tools

by

Nathan Tessema Ersumo

A report submitted in partial satisfaction
of the requirements for the degree of

Master of Science

Committee:
Professor Rikky Muller, Chair
Professor Laura Waller, Co-Chair

Electrical Engineering and Computer Sciences
University of California, Berkeley

Fall 2020

A Modular Design Framework for the Systematic Development of Primitive, Application-Specific Optical Modulation Tools

by Nathan Tessema Ersumo

Research Project

Submitted to the Department of Electrical Engineering and Computer Sciences, University of California at Berkeley, in partial satisfaction of the requirements for the degree of **Master of Science, Plan II**.

Approval for the Report and Comprehensive Examination:

Committee:

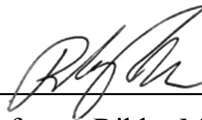

Professor Rikky Muller
Research Advisor

09/15/2020

(Date)

* * * * * * *

Professor Laura Waller
Second Reader

9/4/20

(Date)

Acknowledgements

First, I would like to thank my partner Nicole Ersaro, who reads every draft I write and tries (sometimes unsuccessfully) to curb my proclivity for unwieldy sentences. Without her, my life would be thoroughly mundane. I would also like to thank Cem Yalcin, who turned out to be an excellent friend on top of being a great research colleague with an infectious level of enthusiasm throughout this ongoing project. I'm grateful to Anthony Abel, whose enduring friendship saw us through our undergraduate years at Drexel, our graduate years at Berkeley, and my wedding to Nicole amidst a pandemic. As always, I would like to thank my parents, Prof. Tessema Ersumo and Azeb Mulatu, as well as my sister, Amiel Ersumo: their sacrifices and support are the foundation upon which all of my past and future achievements are built. On a professional note, I would like to thank Dr. Nick Antipa, Prof. Nicolas Pégard, Dr. Daniel Lopez, and Prof. Ming Wu for technical contributions, helpful discussions, and equipment access. I'm grateful to Prof. Laura Waller for access to testing resources and for serving as a reader for this report. And lastly, I would like to thank my adviser Prof. Rikky Muller for her ongoing mentorship, support and supervision of this work. Parts of this report were adapted from [1], a conference proceeding of this work.

Abstract

High-speed primitive optical modulation is widely employed across applications in microscopy, material processing, adaptive optics and augmented/virtual reality. Despite this ubiquity, the embodiments of specific optical modulation tools may vary considerably as a result of the specific performance needs of each application. We present here a consolidated modular framework for the systemic design of high-speed ($\approx 10\ kHz$) array-based optical modulation devices requiring limited degrees of freedom ($\approx 10^1 - 10^2$). The proposed framework combines a semi-custom commercial fabrication process with a comprehensive simulation pipeline in order to optimally reconfigure pixel wiring schemes for the efficient allocation of available degrees of freedom. By decoupling the pixel-level building blocks determining transduction characteristics from the array-scale partitioning geometry determining overall optical functionality, the framework is able to produce tailored array-scale designs that are both robust to process variations and easily reconfigurable for adaptation to alternative specifications. As a demonstration of this framework, phase-shifting piston-motion parallel-plate capacitive micromirrors were designed and fabricated in small array formats for preliminary assessment and characterization under MEMSCAP's standard PolyMUMPs process. Once a suitable micromirror structure was identified, an axial focusing array with a simulated optical power range of ± 2.89 *diopters* was subsequently designed via an iterative ring partitioning process and a Monte Carlo-based simulation pipeline that accounted for experimentally measured spatial variations in pixel performance.

Table of Contents

List of figures and tables **ii**

1 Motivation and background **1**

2 Proposed modular framework **4**

2.1 Technology landscape: key metrics and considerations 4

2.2 Proposed design methodology 7

2.3 Building block selection 9

3 Pixel-level design process **12**

3.1 Overview of pixel-level computational environment 12

3.2 Selected fabrication platform 17

3.3 Assessment of fabricated structures 20

4 Array-level design process **23**

4.1 The impact of spatial variation 23

4.2 Overview of array-level computational framework 25

4.3 Simulated performance results 30

5 Discussion and conclusions **32**

References **34**

Figures

1.1 Primitive phase shifting profiles 2

2.1 Flowgraph of micromirror-based design approach 9

3.1 3D rendering of micromirror structure 13

3.2 Overview of pixel-level simulation results 17

3.3 Scanning electron microscopy images of fabricated micromirror structures . . 19

3.4 Assessment of small-format arrays 22

4.1 Performance comparison between shielded, large-format arrays and unshielded, small-format arrays 24

4.2 Simulation pipeline for axial focusing array. 29

4.3 Simulation results for designed axial focusing array 31

Tables

2.1 Comparison of high-speed axial focusing technologies 6

1. Motivation and background

The development of advanced optical techniques in recent years for the recording, manipulation, processing or reproduction of volumetric objects has precipitated a surge of interest in tools that can dynamically sculpt light. While these needs may broadly be tackled with full-fledged spatial light modulators (SLMs) that provide arbitrary phase control across a given plane [2], such tools typically require $\approx 10^6$ addressing channels and offer $\approx 10^2$ Hz speeds. Full-fledged SLMs are therefore too burdensome or slow for higher speed optical manipulation that only requires a limited number of degrees of freedom (DoF) [3]. As shown in Figure 1.1, a significant portion of the light sculpting tasks performed in practice simply involve the application of primitive phase profiles. General examples include (a) profiles that vary along a single cartesian axis, such as ones used for beamsteering or 1D focusing [4], (b) circularly symmetric profiles that vary with radius, such as ones for 2D focusing [4], spherical aberration correction [5] and conical phase shaping for Bessel beam formation [6], and (c) profiles that vary with polar angle, such as spiral phase profiles used to generate optical vortices [7]. Unlike arbitrary phase profiles, which require high spatial precision in phase control, the primitive phase profiles illustrated in Figure 1.1 are more robust to noise-like deviations from desired phase because collapsing the required number of DoF increases the area of elemental regions subject to phase control. Whether standalone or cascaded together, tools that produce such fundamental phase shift patterns enable routinely employed optical functionalities including 3D scanning, laser beam shaping and simple aberration correction. These tools are thus widely applied in fields including astronomy [8], biological microscopy [9], optical trapping [10], ophthalmoscopy [11], and augmented reality/virtual reality (AR/VR) [12].

Despite this ubiquity, specific embodiments of primitive optical modulation tools vary widely

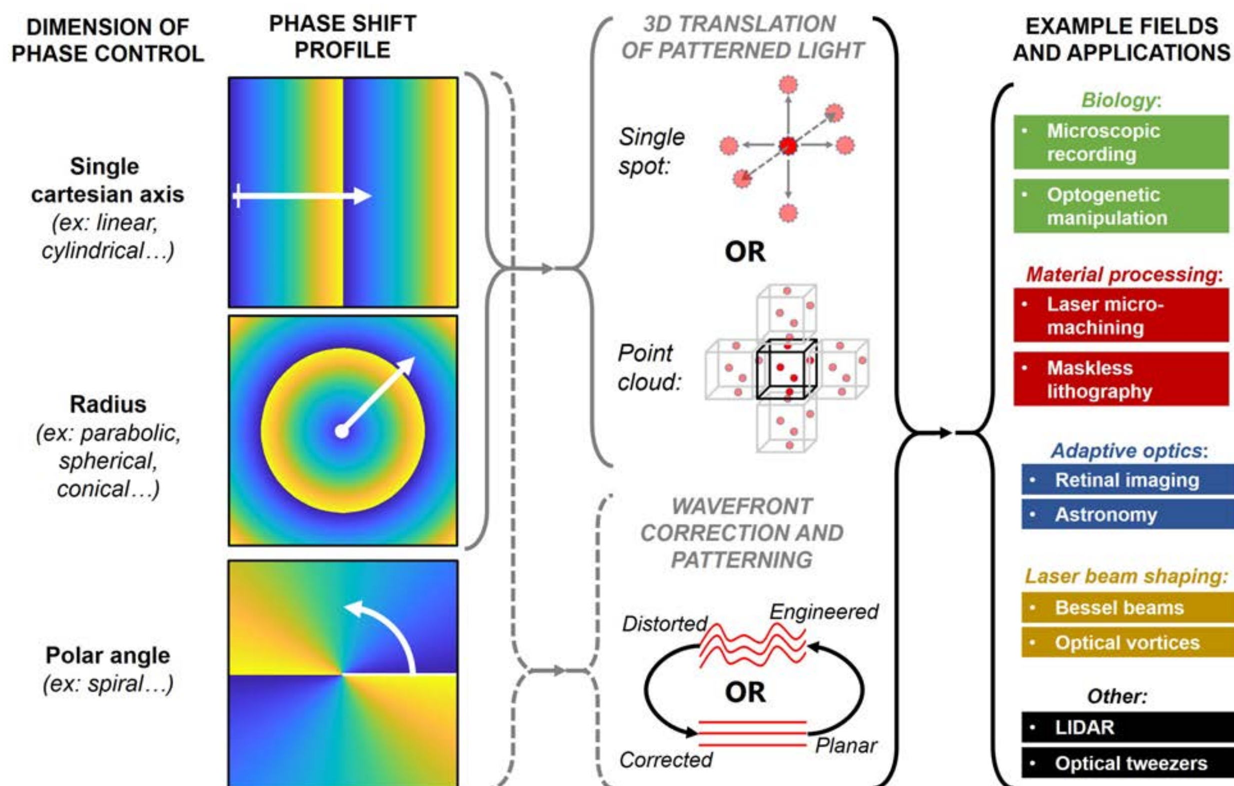

Figure 1.1: Primitive phase shifting profiles, including ones that are constant along one cartesian axis, ones that are circularly symmetric, and ones that are radially uniform, are used in a wide variety of applications across several fields. While the optical functionality enabled with such phase profiles typically involves some combination of 3D scanning, adaptive optics or waveform engineering, exact performance needs remain highly application-dependent.

in accordance with the diversity in performance needs across applications: different applications require different combinations of these fundamental phase modes and different extents of control for each mode. For instance, while the 3D translation of patterned light generally requires three DoF, i.e. phase control of the cartesian axis x, cartesian axis y, and polar radius r, 3D scanning tools cannot easily be adapted for applications with diverging requirements on resolution and range across X, Y and Z dimensions of the target volume. Accordingly, $X-$, $Y-$ and $Z-$scanning tools tailored for single-cell resolution biological microscopy [13] would not, for example, efficiently address the macro-scale target volumes of LiDAR surveying [14] or the axially-compressed aspect ratios of lithography [15]. Moreover, considerations relating to wavelength of operation and optical power requirements place additional constraints on

efforts to repurpose existing optical modulation tools. Altogether, the simultaneously prevalent and application-specific nature of optical modulation tasks with limited DoF has resulted in an explosion of off-the-shelf products, from galvanometers [16] and acousto-optic deflectors [17] to tunable lenses [18] and radially curving mirror plates [19], [20], that make use of various technologies including electrowetting [21], elastomeric deformation [22] , liquid crystals [23], acoustic gradients [24] and micro-electromechanical systems (MEMS) [19]. Though these myriad commercial offerings and modulation approaches expand available options for any optical modulation task, off-the-shelf solutions rarely represent the most efficient embodiment of a given task for a given system and application. The application-specific nature of spatial light modulation tasks often results in inefficiencies for such fixed-format tools, with either (a) insufficient levels of control and precision being allocated the most critical DoF, or (b) excess DoF that go wasted and create undesired operating overhead. In order to provide maximal tailorability for these tools while ensuring accessibility by minimizing development efforts and cost, we propose a computational framework that allows for the systematic design or reconfiguration of nimble optical modulation devices requiring limited DoF by making use of array-based modularity. With this framework, full-fledged arbitrary spatial light modulation can easily be whittled down into desired application-specific tools by efficiently consolidating available DoF in a manner that is highly tailored to specific performance needs yet minimizes operating overhead. While this framework can be complemented with any fabrication platform, we illustrate a successful design iteration and experimentally demonstrate the framework's viability using a standard MEMS fabrication process and phase-shifting micromirrors as building blocks. A key feature of the proposed framework is the decoupling of the design and analysis of the unit elements that determine transduction characteristics from the array-scale geometry that determines overall optical functionality. With this feature, we anticipate that our framework will power the development of a library of architectures that can easily be reconfigured and built to specification in the same way that passive optical elements such as lenses can be custom-fabricated.

2. Proposed modular framework

2.1 Technology landscape: key metrics and considerations

To first illustrate how the proposed unified framework can eliminate mismatches, inefficiencies, and bottlenecks in optical manipulation systems, we examine key metrics and performance tradeoffs at play for one specific example of optical manipulation: dynamic axial focusing. Two important considerations for this common subtask are that it is often implemented in conjunction with lateral scanning capabilities for 3D scanning [13] and that it typically introduces target depth-dependent spherical aberrations that require correction [5]. Yet while state-of-the-art lateral scanning tools including galvanometer mirrors and acousto-optic deflectors boast refresh rates in excess of 5 kHz (under dwelling-capable non-resonant operation) [25], some of the most widely used and commercially available axial focusing tools today are not able to match these speeds. Indeed, dynamic optofluidic lenses [26] and liquid crystal-based devices [27] operate at refresh rates that are well under 300 Hz. Accordingly, efforts have been made to increase axial focusing speeds to refresh rates of up to 1 MHz by employing alternative technologies as shown in Table 2.1. But these improvements have come at the expense of crucial capabilities. Specifically, continuous deformable mirror arrays (cDMs) [28] and electro-optic deflectors (EODs) [25] require very high voltage drives and/or numerous addressing channels that entail cumbersome amplifiers, precluding the possibility of compact driver integration. Furthermore, tunable acoustic gradient index of refraction (TAG) lenses [24] are continuously sweeping across Z, which means that laser syncing is required and dwelling is not possible. Alternatively, strategies such as cascading acousto-optic deflectors (AODs) [25], [29] or producing binary Fresnel zone plates with digital micromir-

ror devices (DMDs) [30] drastically reduce transmission efficiency. Cascaded AOD systems also suffer from decreasing dwelling capacity with increasing deflection as well as a limiting tradeoff between axial and lateral scanning ranges. In addition, monolithic MEMS mirror plates require resonant-mode operation for meaningful operating ranges, which severely limits performance under dwelling-capable non-resonant modes [20]. And lastly, most of these approaches to axial focusing provide no additional control over radial phase curvature for a given target depth, constraining their ability to address target position-dependent aberrations and thereby limiting the ease with which they can be fully adapted to various systems.

Table 2.1: Comparison of high-speed axial focusing technologies. cDM: continuous deformable mirror. DMD: digital micromirror device. EOD: electro-optic deflector. AOD: acousto-optic deflector. TAG: tunable acoustic gradient index of refraction. RF AM: radio frequency amplitude modulation.

	cDM array [28]	**DMD zone plates** [30]	**EOD lens** [25]	**Cascaded AODs** [25], [29]	**TAG lens** [24]	**Monolithic MEMS** [20]
Response rate	$1 - 50\ kHz$	$50\ kHz$	$1\ MHz$	$1\ MHz$	$100\ kHz$	$> 100\ kHz$
Driving range	$250\ V$	$2\ V$	$\pm 150\ V$	$5\ V$ (RF AM)	$50\ V$	$> 30\ V$
Driving channels	$\approx 10^3$	$\approx 10^6$	1	$3 - 4$	1	1
Transmission efficiency (%)	> 90 %	≈ 1 %	$60 - 80$ %	6.25 %	> 90 %	> 90 %
Polarization dependence	No	No	Yes	No	No	No
Dwelling capacity	Yes	Yes	Yes	Limited	No	Limited

More broadly, state-of-the-art solutions to optical manipulation needs sacrifice either critical performance capabilities (in the form of efficiency, polarization dependence, wavelength range, dwelling capacity, etc.) or operating overhead (in the form of voltage range, number of driving channels, and power consumption). Limitations relating to this general tradeoff are especially salient when multiple kinds of spatial light modulation are cascaded together as mismatches across performance metrics result in bottlenecked and cumbersome operation. Therefore, the first mandate governing the development of the proposed unified design

framework is that operating overhead should be made commensurate to the extent of optical manipulation that is required: this entails a consolidation process whereby available DoF are efficiently allotted as part of the framework's design iteration. The second mandate is that multiple tools aimed at different tasks and generated from separate design iterations under this framework can be efficiently cascaded together for expanded performance without the introduction of performance mismatches. The best way to achieve this feature would be to introduce modularity to the framework such that tools destined for different tasks can still comprise identical building blocks that determine transduction characteristics. Overall, the most straightforward approach to satisfying these two mandates is to structure the proposed framework as a vector space with an orthogonal basis set of pixels, i.e. unit elements corresponding to all available DoF and defined by distinct positions. These unit elements can then be tiled, consolidated, partitioned and replaced in a systematic way across a prescribed region that becomes the active area of the designed spatial light modulation tool.

2.2 Proposed design methodology

We propose an object-oriented array-format design approach to optical modulation tools that decouples the building blocks (i.e. pixels) determining transduction characteristics (ex: applied drive vs. achieved phase shift, settling behavior, etc.), from the array-scale geometry determining overall optical functionality as shown in Figure 2.1(a). This modular design scheme is achieved by fixing the pixel tiling pattern and adjusting grouped wiring schemes between pixels. Once the pattern and pitch of the array tiling scheme is set, pixels may be selectively added or removed in accordance with this scheme across a 2D working area that is agnostic to the unit pixel's structure. First, such a decoupled analysis strategy between unit actuator structure and array configuration provides freedom in setting the transduction mechanism and its balance between spatial uniformity and sensitivity without affecting the array-level phase coordination strategy that determines optical performance. Depending on

the application, the unit actuator pixel may be easily switched out within the modular design framework to structures that rely on particular mechanisms of optical manipulation such as amplitude modulation [31] or diffraction order-specific phase modulation [32]. Second, compared to larger monolithic structures, partitioning active areas into co-wired grouped regions and again into small pixels typically provides improved speed and transduction sensitivity (especially for mechanical structures) [33], the ability to phase-wrap applied patterns for extended operating ranges, and mitigation against the non-idealities and instabilities that plague allowable phase modes across larger structures [34], [35]. Third, while segmented pixels are susceptible to diffraction effects that can introduce unwanted static and dynamic diffraction orders as well as reduce zeroth-order efficiency commensurately with the square of array fill factor [36], such segmented arrays can be operated in optical setups that eliminate these undesired effects via static illumination patterning and spatial filtering as shown in Figure 2.1(b). Overall, the design process under this framework thus becomes a matter of iteratively reducing the basis set of addressable elements from an expansive initial orthonormal set representing full-fledged arbitrary spatial light modulation to a reduced set that eliminates wasted DoF. The only requirement on the selection of pixel building blocks and fabrication platforms to complement this framework is that they must physically accommodate a straightforward and systematic wiring process that mirrors the tiling and partitioning steps of the computational framework.

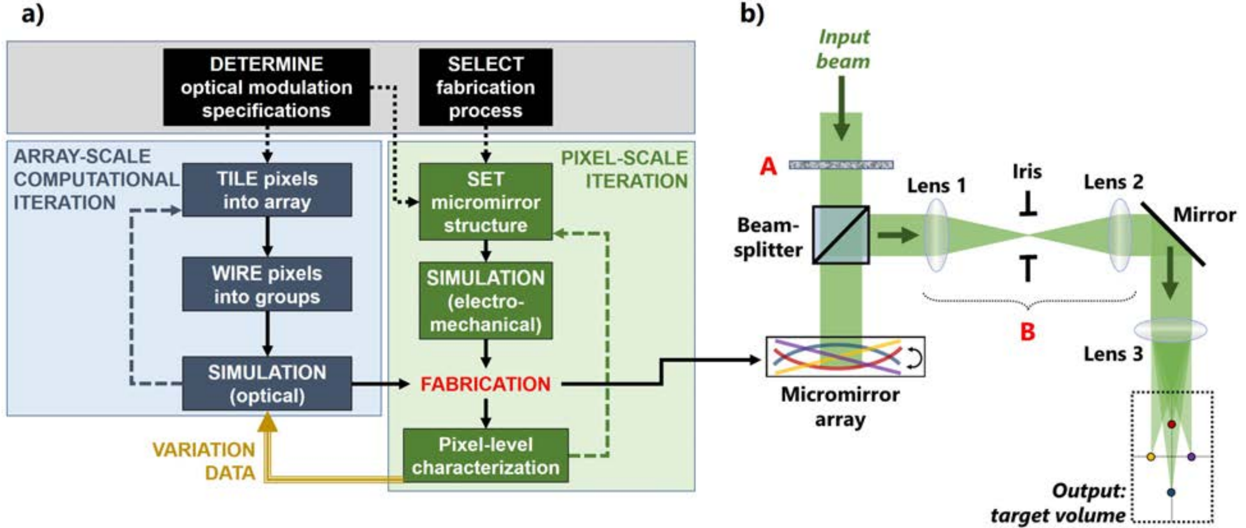

Figure 2.1: a) Flowgraph illustrating micromirror-based design approach to optical modulation tools. Once the target tool specifications and fabrication platform are set, pixel-scale and array-scale design iterations can be decoupled for a modular development process. b) Envisioned optical system for arrays produced under this framework. A binary amplitude mask (A) may be used to illuminate only active areas of the employed array and a spatial filter (B) can be employed to prevent unwanted diffraction orders from appearing around the volume of interest.

2.3 Building block selection

Given the versatility of the proposed framework in the selection of the pixel-level transduction mechanism and geometry, a survey of past periodic optical modulation structures is warranted in order to pick dynamic building blocks that can best demonstrate the viability and utility of this framework. Kilohertz-rate speeds are typically desired in biological microscopy, where relevant dynamics such as neural signaling occur at millisecond timescales [13], and in AR/VR, where 3D image generation techniques seek to maximally exploit the 1 kHz detection rate of the human eye [37]. As evidenced by the popularity of galvanometers for lateral scanning and the axial focusing technologies listed in Table 2.1, the prevailing approach to increasing optical modulation speeds involves employing mechanical methods to actuate mirrors. Settling times for such systems are determined by mechanical resonant

frequency, which scales with $\sqrt{\frac{k}{m}}$ (where k and m are respectively the spring constant and dynamic mass of the actuation mode of interest). By exploiting the surge in resonant frequency that comes from shrinking down to MEMS scales, micromirror structures can achieve refresh rates of 10 kHz or higher [33]. Broadly, mirror-based optical tools can be classified into monolithic structures (ex: galvanometers and varifocal plates) and multi-actuator arrays. Larger monolithic structures benefit from the simplest driving schemes but provide limited additional control and often rely on resonant-mode operation due to the high drive required of DC operation. On the other hand, the expanded functionality offered by multi-actuator arrays, also known as micromirror arrays or deformable mirror arrays, has drawn considerable interest which has led to the development of various design iterations over the years [28], [33]. Examples of such iterations have included tip-tilt mirrors for pixel-level beamsteering [38], piston-motion mirrors for pixel-level phase shifting [39], [40], ribbon-like mirrors that produce 1D phase profiles [4], and lateral mirror gratings that produce diffraction order-specific phase shifting [32]. However, uniformity issues relating to spatial variations in fabrication processing have constrained commercially viable micromirror array designs capable of reliable optical modulation to two general subtypes. The first subtype, which corresponds to the widely employed DMDs, restricts micromirrors to binary operation, i.e. on/off amplitude modulation, which reduces voltage drive enough to achieve pixel counts on the order of 10^6 but sacrifices analog control of each pixel [30]. The second subtype, which corresponds to cDMs, offers analog tip, tilt and piston control by creating highly-rigid suspension schemes that ensure uniform performance at the expense of inter-actuator coupling and high voltage drives that reduce viable pixel counts down to $\approx 10^2 - 10^3$ [41]. Yet since our proposed framework inherently relies on the averaged performance of hundreds of pixels by consolidating $\approx 10^3 - 10^6$ pixels per tool into $\approx 10^1 - 10^2$ actuation channels via co-wiring, the need for high spatial uniformity is obviated: rigidity and driving voltage requirement can therefore be relaxed without compromising optical functionality. Accordingly, as part of this work, we illustrate the pixel-level design process of the framework by designing low-rigidity

micromirror structures that are best suited for optical modulation tasks requiring limited DoF. We have chosen piston-based parallel-plate capacitive transduction as the actuation mechanism for the designed mirror. This mechanism provides full (2π) control over a fundamental optical modulation parameter (phase) across a wide range of wavelengths using a single mechanical deformation mode, simple open-loop DC voltage drive and only one electrode pair per actuation channel.

3. Pixel-level design process

3.1 Overview of pixel-level computational environment

The pixel-level design iteration process involves a preliminary first-order design and analysis using an analytical framework followed by finite element simulation to assess steady-state and dynamic transduction behavior. A piston-motion parallel-plate capacitive micromirror typically involves a mirror body acting as an electrode suspended over a parallel fixed electrode plate with a finite number of suspension beams that are each anchored to the substrate on one end and attached to the mirror body at the other end, as shown in Figure 3.1. Since the piston-type mechanical mode only results in the translation of the mirror body along the direction that is normal to the substrate plane without any torsion, rotation or lateral motion, the suspension beam is characterized by a guided boundary condition at the mirror end and a clamped boundary condition at the anchor end. Suspension beams must be arranged such that the net moment experienced by the mirror body is zero: this typically entails an axially symmetric configuration around the center of the mirror plate. The application of a non-zero, positive DC voltage across the two electrodes of the pixel structures produces an attractive electrostatic force that pulls the suspended mirror body closer to the fixed electrode. The resulting net displacement of the reflective mirror surface from its resting plane adds double this displacement value to the travel path of locally incident light, thus imparting a pixel-level optical phase shift that depends on the light's wavelength. The balance between the rigidity, i.e. spring stiffness, of the beams (set by the beams' geometric dimensions) and the magnitude of the electrostatic force (set by the parallel plate's area and gap size) determine the steady state relationship between displacement and applied voltage. Since parallel-plate voltage-drive transduction triggers pull-in once displacement exceeds one

third of the original gap distance, the electrode gap size must be over 1.5 times greater than the maximum optical wavelength desired for operation. Since most applications involving optical manipulation span UV (ex: maskless lithography [40]), visible (ex: AR/VR [12]), and even near-infrared (ex: multiphoton microscopy [42]) wavelength ranges, we set 1 μm as the reference wavelength for the design iterations illustrated in this work.

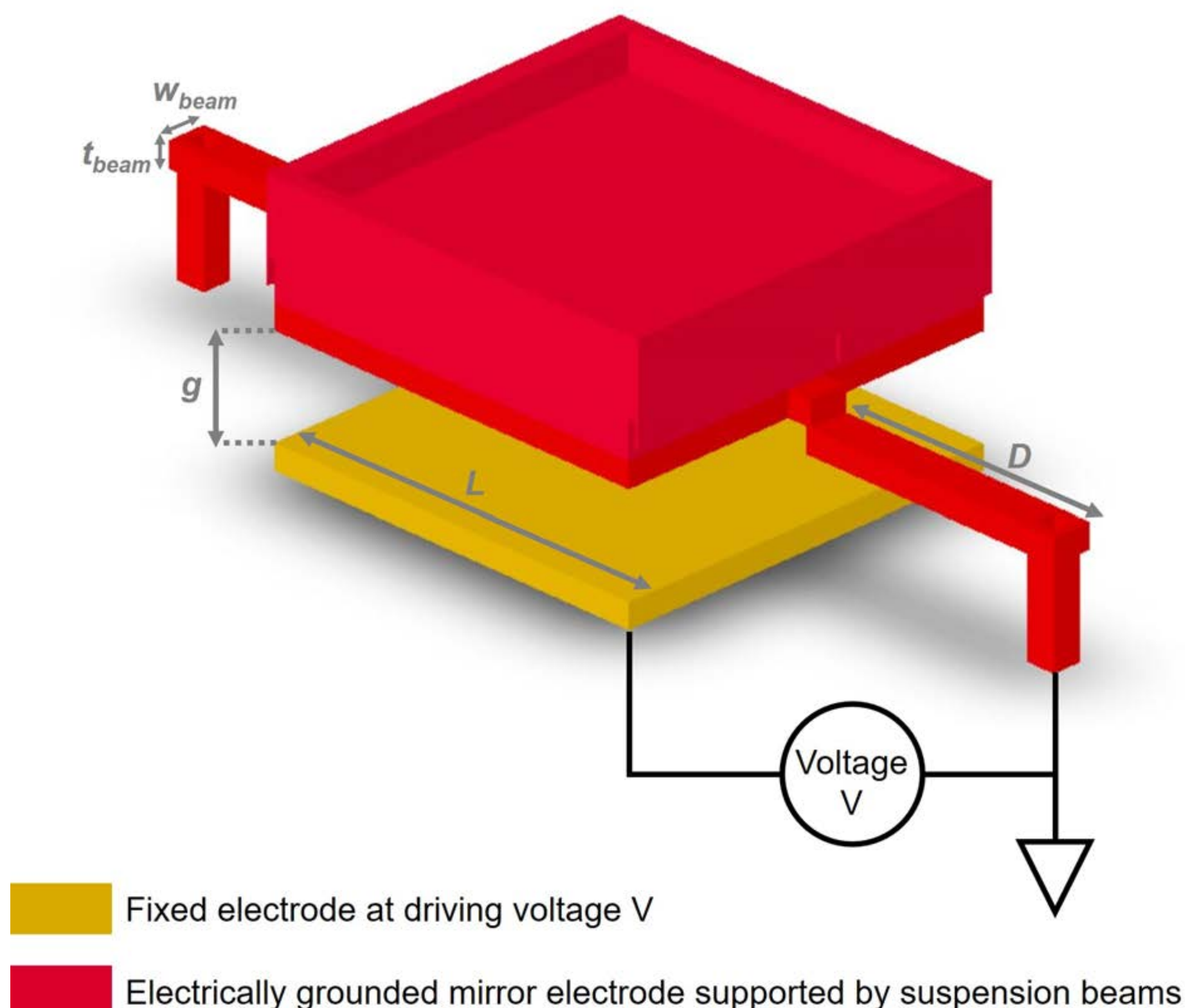

Figure 3.1: 3D rendering of example square-format micromirror structure supported by N=2 suspension beams. Annotations are included for critical dimensions and parameters governing micromirror performance.

Assuming that damping force is proportional to plate velocity, and that the beams act as a linear spring, the analytical model for mirror behavior was derived based on the following force balance ordinary differential equation:

$$F_{el} - b\,\dot{\Delta x} - k\,\Delta x = m\,\ddot{\Delta x}$$

F_{el} corresponds to the attractive electrostatic force between the two electrodes, b is the damping coefficient in the fluid medium, k is the spring constant of the suspension beams and Δx corresponds to vertical plate displacement (axis is oriented downwards towards the substrate and $\Delta x = 0$ at the resting plate position). Assuming that the parallel plate electrodes are square-shaped, the employed damping coefficient b was obtained from a previous analytical derivation of squeeze film damping using the Navier-Stokes equation and assuming a low Reynold's number [43]. For a non-perforated square plate of side length L, film gap g and a fluid viscosity of μ, the damping coefficient b is given by:

$$b = 0.422\,\frac{\mu\,L^4}{(g - \Delta\,x)^3}$$

The generated electrostatic force is given by the equation:

$$F_{el} = \frac{1}{2}\,\epsilon\,V^2\,\frac{(L_{EFF,CAP})^2}{(g - \Delta\,x)^2}$$

where ϵ is the permittivity of the fluid medium separating the electrodes and V is the voltage applied across the electrodes. We note that $L_{EFF,CAP}$ is the effective side length of the overlapping area between the two capacitor plates $L_{EFF,CAP} = L$ if the square plates are identical and perfectly overlap). In addition, the employed spring constant was obtained based on the assumption that the N suspension beams supporting a given mirror are geometrically identical and constitute parallel clamped-guided beams of rectangular cross-section with height

t_{beam} and width w_{beam} [44]:

$$k = \frac{N\,E\,(t_{beam})^3\,w_{beam}}{D^3}$$

where D is beam length whereas E is the Young's modulus of the beam material. This relationship also holds if the suspension architecture is a single clamped-clamped beam attached at its midpoint to the mirror body since such a beam is equivalent to two clamped-guided beams of length D which corresponds to half the length of the full beam. Finally, the effective mass undergoing acceleration was comprised of the entire mass of the mirror body (including its reflective metal layer) as well as one third of the mass of the spring beams:

$$m = \rho_{structure}\left(V_{mirror\,body} + \frac{N\,t_{beam}\,w_{beam}\,D}{3}\right) + \rho_{metal}\,V_{metal}$$

where $\rho_{structure}$ is the density of the material forming the beams and mirror body, ρ_{metal} is the density of the metal used as a reflective layer, $V_{mirror\,body}$ is the total volume of the mirror body, and V_{metal} is the total volume of the reflective metal layer. Using the listed equations, parametric `MATLAB` scripts were developed to calculate plate displacement over time for a given applied voltage as well as the required voltage to be applied for a given displacement. Specifically, `ODE45`, a numerical Runge Kutta solver, was employed to obtain mirror behavior after the application of a single step voltage drive from an initial condition of zero displacement and zero velocity.

Though the described analytical model was used to guide the first-pass selection of design parameter values (namely pixel-level geometric dimensions), we note that it fails to account for certain higher-order phenomena that play a significant role in mirror response. Regarding settling behavior, the analytically obtained damping coefficient b was derived based on the assumption that there is ambient pressure at the edge of each mirror. Yet given the densely packed nature of the mirrors across a given array, there will likely be pressure buildup

at mirror edges which may even spill over into surrounding mirrors. More importantly, the developed model does not incorporate the impact of fringing fields (both within an isolated mirror and between adjacent mirrors) nor does it recapitulate the true behavior of the supporting beam, which is a non-linear spring subject to both strain stiffening and residual stress effects. In addition to modulating spring stiffness and causing suspension beam buckling, stress mismatches and gradients can also cause suspended mirrors to curl since a mirror body and its reflective metal layer amount to a bimorph structure. In order to evaluate the impact of these higher-order effects, design parameters and analyses were finalized using finite element models constructed in `CoventorWare`. 3D models of pixels were constructed by defining fabrication process steps and mask layouts, after which steady state electromechanical studies, damping studies and eigenfrequency studies were run to obtain displacement vs. voltage behavior, settling response behavior and mechanical resonance behavior, respectively as shown in Figure 3.2.

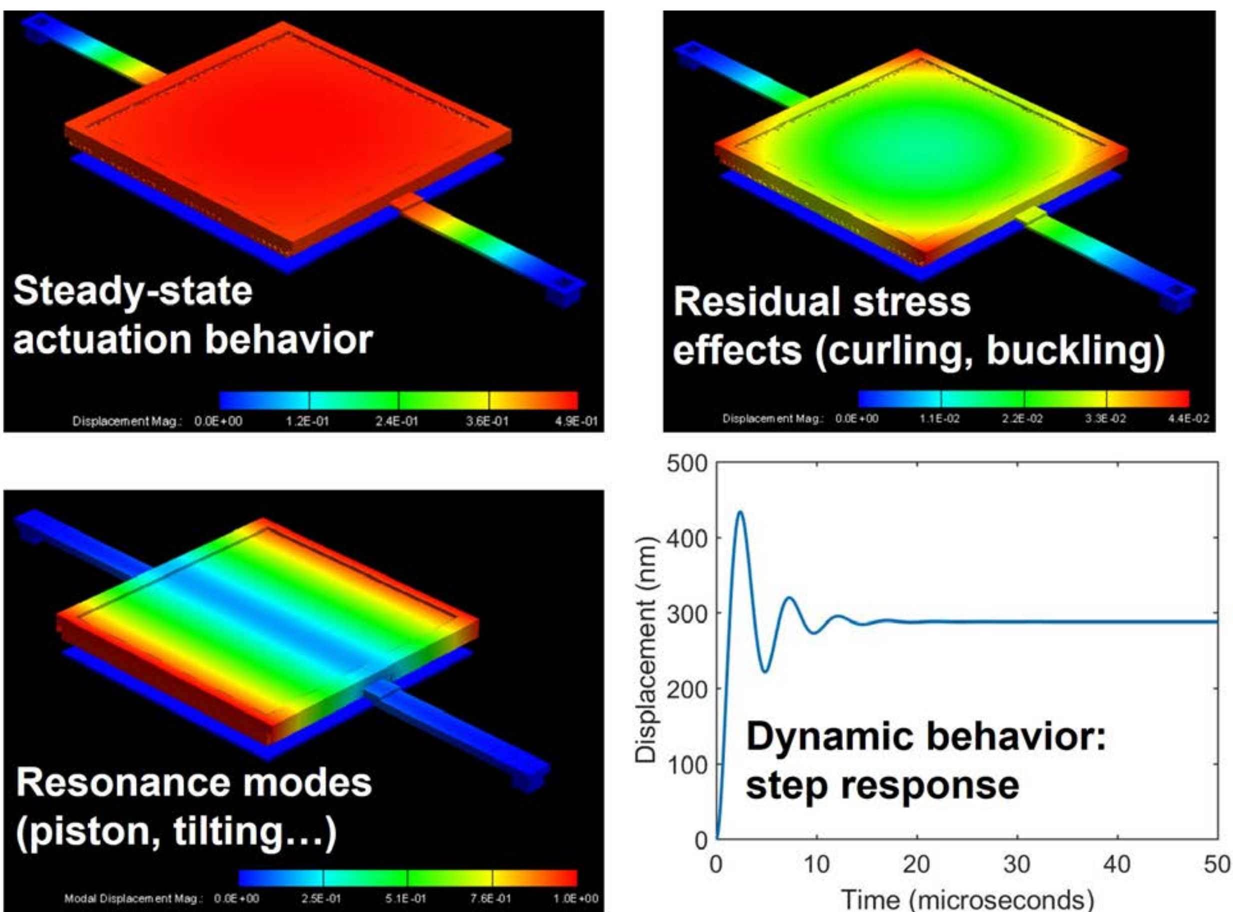

Figure 3.2: Overview of simulation results from pixel-level analytical and finite element simulation frameworks.

3.2 Selected fabrication platform

Since the pixel-level design process is framed by the imposed constraints and afforded latitudes of the fabrication process, the eventual utility of the proposed computational framework is contingent on the complementary nature of the selected fabrication platform. Specifically, the chosen fabrication platform must provide a level of accessibility and reliability that is suitable for systematic redesign as well as a level of versatility and flexibility that can accommodate the modularity of the framework. To this end, we selected MEMSCAP's Multi-User MEMS Processes (MUMPs), specifically the PolyMUMPs standard process in

conjunction with the MUMPs-PLUS semi-custom modification service, to experimentally illustrate the viability of our framework. Employing PolyMUMPs, a straightforward and commercial process that involves the deposition of three structure polysilicon layers interleaved with two sacrificial oxide films on a nitride-coated single crystal silicon substrate [45], will serve to demonstrate that viable micromirror building blocks can be reliably produced without the need for intricate, advanced, burdensome or costly processing. And with the addition of the MUMPs-PLUS service, which offers the option of marginal modifications to layer thicknesses, materials and process sequencing, the base PolyMUMPs fabrication platform is outfitted with a level of tailorability that mirrors the modularity of building blocks in the design framework. Using this MUMPs-PLUS service, the thickness of the middle polysilicon layer (Poly1) was reduced from 2 μm down to 500 nm in our fabricated arrays in order to alleviate micromirror suspension rigidity and reduce voltage drive requirements.

While the described platform provides enough structural versatility to support the development of various mechanical suspension, actuation, tiling and wiring schemes, we recognize that a single standard process step cannot accommodate the wide diversity of application-specific performance requirements for the mirror surface, including its spectral reflectance, polarization handling, optical power limit, and sensitivity to angle of incidence. We therefore envision reflective layer deposition as a separate post-processing step performed in-house or by a specialized foundry, whereby structures comprising metals, photonic crystals, dielectric stacks or metamaterials are patterned on top of fabricated mirror bodies via techniques including evaporation [46], sputtering [47], additive manufacturing [48], and e-beam lithography [49], [50]. Accordingly, in-house post-processing involving the evaporation and lift-off patterning of a 250 nm-thick gold layer was performed to impart adequate reflectivity to our fabricated array pixels. Employing this method instead of the standard 500 nm gold metal evaporation offered as part of the PolyMUMPs process serves the dual purpose of illustrating the feasibility of custom post-processing for the deposition of reflective layers and minimizing the likelihood of mirror curling due to residual stress mismatches.

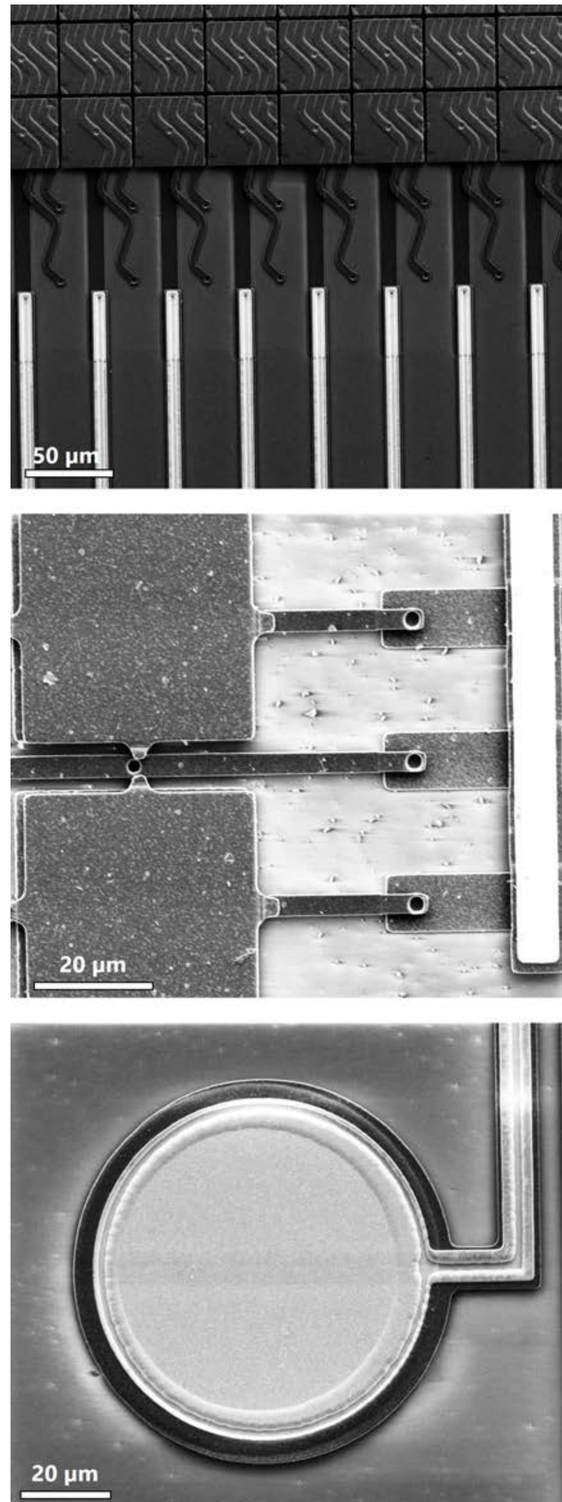

Figure 3.3: Scanning electron microscopy (SEM) images of fabricated micromirror structures illustrating implemented wiring schemes for pixel partitioning. Top: separately partitioned columns of type A micromirror pixels. Middle: co-wired group of 3 rows of type B micromirror pixels. Bottom: wiring traces are routed to separate bond pads.

Scanning electron microscopy (SEM) images of two types of fabricated, tileable micromirror structures (A and B) prior to reflective layer deposition are shown in Figure 3.3. The wiring process that parallels the pixel partitioning process in the computational design framework is carried out under the same systematic layout-level approach for both pixel structure types. Electrical connections between adjacent pixels within an array are selectively made by adding or removing a finite number of connection points between fixed electrodes in the Poly0 routing layer. At the edges of the array, gold metal traces are then routed out to gold pads which are bonded out for on-board connection to independent voltage drivers. Similarly, mirror bodies in a given array are co-wired together via shared suspension beam anchors and nitride breaches into the substrate, then routed out via gold traces to a ground connection.

3.3 Assessment of fabricated structures

Following reflective layer deposition and release, the array uniformity of fabricated structures was assessed visually under differential interference contrast microscopy as shown in Figure 3.4(a). The examination of small-format (i.e. 10x10 or 10x20) test arrays, for instance, revealed that both inter-pixel and intra-pixel planarity was considerably better in type B structures compared to type A structures. Given the extensive variation in both tilting and resting height seen across type A structures, type B arrays were chosen for further optical testing. Specifically, a 10x20 array wired into 10 independently addressable rows was driven using ADI AD5535B digital-to-analog converters (DACs) controlled by an Opal Kelly XEM6010-LX150 FPGA. The resulting beamsteering phase ramps were imaged using a Lyncée Tec R1000 digital holographic microscope (DHM) for phase reconstruction under a 675 nm laser wavelength [51]. As shown in Figure 3.4(b), type B pixels were found to behave fairly uniformly at several voltage levels. Functional beamsteering testing was subsequently performed under an imaging setup with a 532 nm laser source. The fabricated MEMS die was outfitted with a custom laser-cut mask to restrict illumination to the beamsteering

array, and placed at the front focal plane of a 100 mm focal length lens, with a CMOS camera positioned at the rear focal plane. Phase ramps were subsequently produced at steps of 0, $\frac{\pi}{4}$, $\frac{\pi}{3}$, and π (i.e. mirror displacement increments of 0 nm, 33 nm, 44 nm, and 133 nm). While the small array format represents a narrow Fourier bandwidth resulting in poor resolution and limited beamsteering performance, the test array was able to successfully and incrementally deflect the zeroth order diffraction spot generated at the camera plane as shown in Figure 3.4(c).

Most notably, producing a phase ramp with a pixel step of π resulted in a deflected spot located halfway between the zeroth order (DC) and first order diffraction spots under uniform phase (i.e. no voltage drive), consistent with the behavior of a binary phase grating. Altogether, this pixel-level development iteration illustrates how the described micromirror design process can be coupled with a standard fabrication platform to produce several small-format arrays, rapidly triage potential building blocks for suitability via inspection and simple functional tests, and perform pixel-level characterization measurements to inform the array-scale design process.

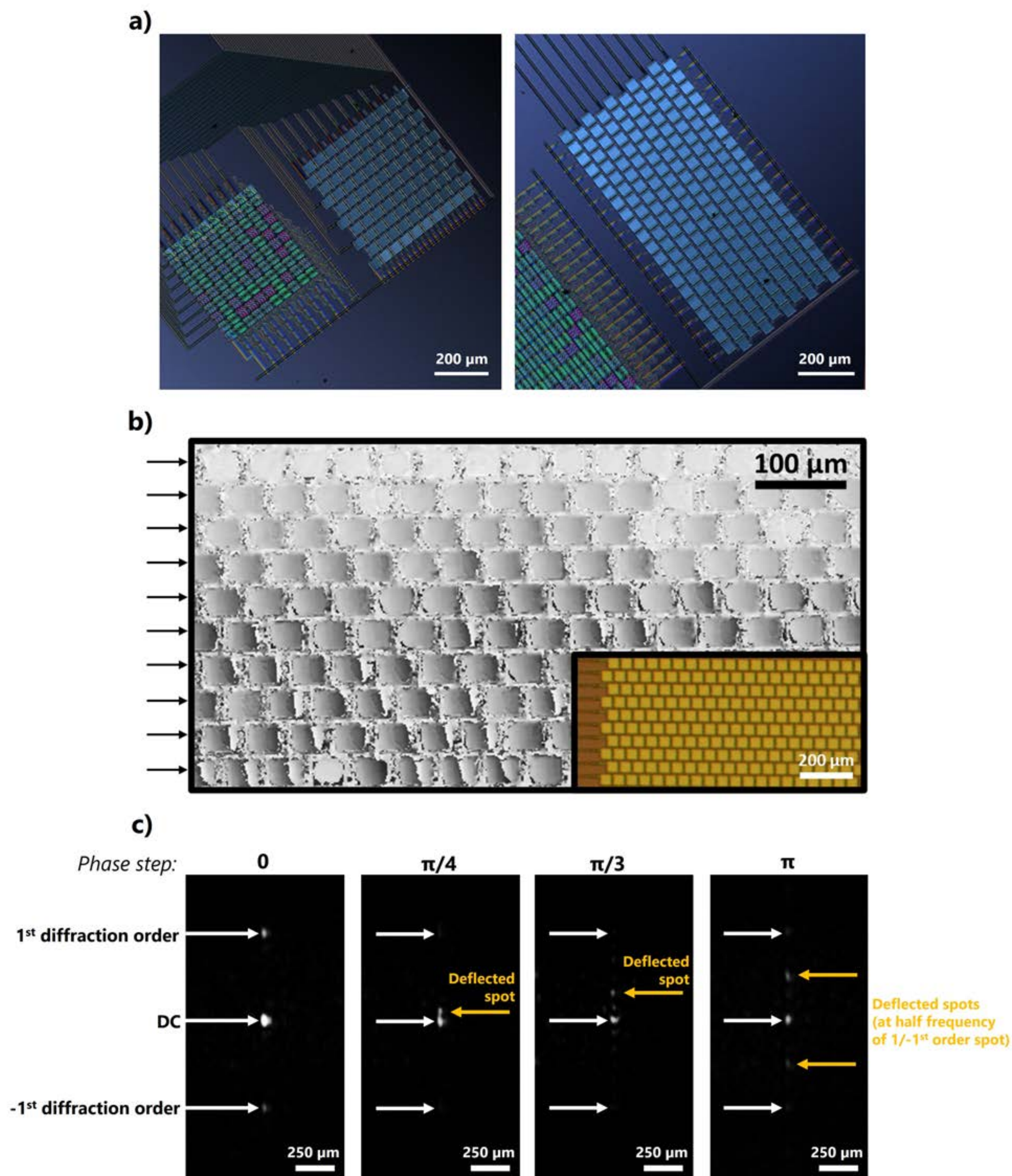

Figure 3.4: Assessment of small-format arrays. a) Differential interference microscopy images of identically tiled and wired type A (left side of each image) and type B (right side of each image) arrays after release. b) Phase reconstruction of sample micromirror array wired into independent rows (as shown with black arrows) and actuated to produce a phase ramp for beamsteering. Microscopy image of array with routing trace to each row shown in bottom-right inset. c) Successful deflection of light spot in an imaging system obtained by producing phase ramps of varying step size using beamsteering array in a).

4. Array-level design process

4.1 The impact of spatial variation

While the pixel-level design process provides insight into expected performance and relative strengths and weaknesses across various structures, spatial process variations during fabrication are often so significant that pixel-level simulations alone cannot reliably guide array-scale design. Experimental post-fabrication pixel-level characterization is therefore typically necessary in order to factor in non-uniformities in pixel performance and accurately predict functional optical performance. The extent to which such variations can lead to deviations in pixel performance is illustrated in Figure 4.1. As seen in Figure 4.1(a), two arrays were laid out and fabricated next to each other, the first one being a large 8.2 mm diameter circular array surrounded by a wall of Poly0 for residual stress shielding, and the second one being a smaller, unshielded 480 $\mu m \times 960$ μm array. Steady state voltage vs displacement measurements performed across pixels of both arrays under DHM and shown in Figure 4.1(b) reveal two kinds of variations. First, spatially continuous variations in geometric properties including layer thicknesses result in regional variations in pixel performance, as evidenced by the wide 95 % confidence interval margins of the larger array and the comparatively uniform pixel performance across the smaller array. Second, non-periodic structures that are peripheral to fabricated arrays (ex: routing traces, shielding walls, substrate breaches and die edges) can significantly modulate the extent and impact of residual stress mismatches. For instance, the observed difference between the 30.4 V mean pull-in voltage of the larger array and the 18.3 V mean pull-in voltage of the smaller array can be attributed to the fact that stress shielding mitigates spring stiffening or softening of the suspension beams in Poly1, which experiences a nominal compressive stress of -10 MPa [45].

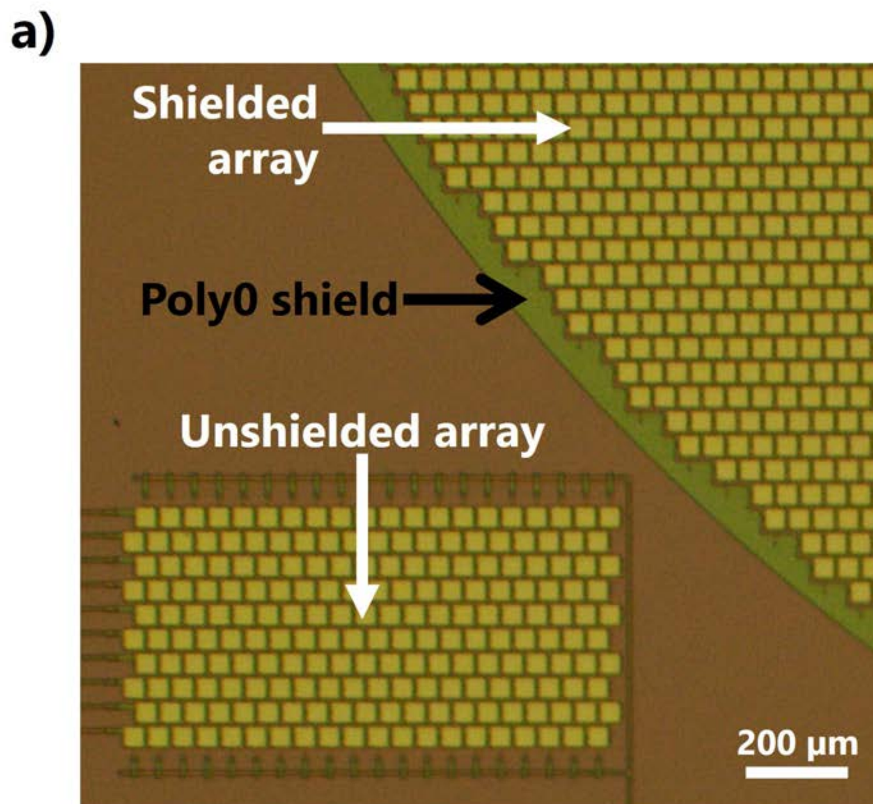

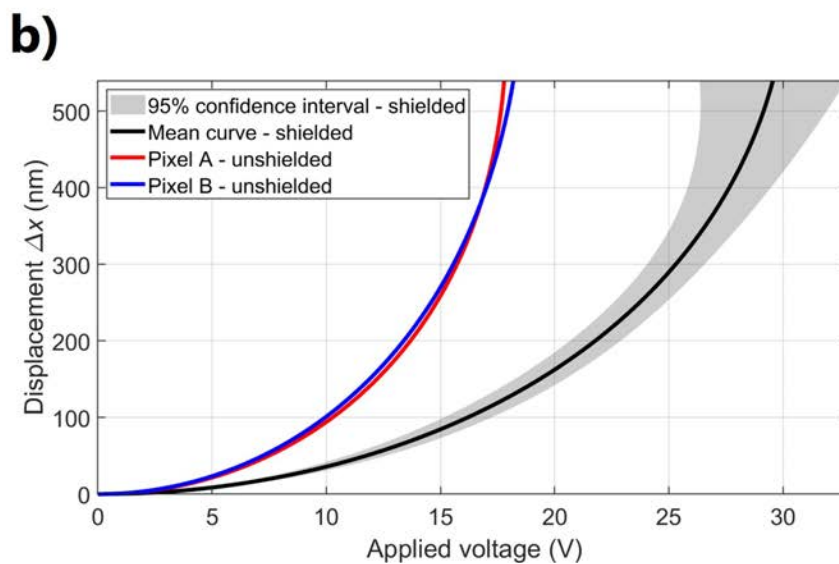

Figure 4.1: Performance comparison between shielded, large-format arrays and unshielded, small-format arrays. a) Pixel-level actuation behavior was measured across two different arrays shown here under microscopy: a protected larger array (top-right) that is shielded from residual stress via surrounding Poly0 layer wall and an unprotected smaller array (bottom-left) that is not shielded with a wall. b) Steady-state displacement vs applied voltage measurements for pixels from protected and unprotected array regions.

Overall, these disparities in pixel performance were experimentally captured under DHM with two types of measurements: variations in resting pixel surface height, which were found to have a standard deviation of 13.83 nm, and variations in actuation-dependent behavior, which were found to have an integrated mean standard deviation of 53.26 nm. The intra-pixel topography of micromirrors was measured under non-contact atomic force microscopy to have a standard deviation of 0.6 nm across 1 $\mu m \times 1$ μm unit areas (relevant to target laser wavelength scales) and was thus found to be negligible at the scale of array-wide functional performance. Therefore, while pixel-level simulation results are sufficient for first-pass array-scale design iterations under idealized assumptions, porting these quantifications of pixel non-uniformity into refined later-stage iterations is crucial to assessing whether the averaging effect of pixel grouping can realistically overcome such non-idealities and ensure adequate optical performance.

4.2 Overview of array-level computational framework

The array-scale design framework was implemented using `MATLAB`'s Image Processing Toolbox as an optical system consisting of an offset lens with the micromirror array plane positioned at the front focal plane and with the target/output volume centered around the rear focal plane. In order to construct an optical test setup that is tailored to a given target application for pertinent simulation results, several system-level parameters must first be defined at the start of any design iteration. These parameters include the focal length f of the offset lens as well as the wavelength λ and complex amplitude profile (ex: Gaussian vs uniform, normally incident vs oblique, amplitude mask defining aperture, etc.) of the coherent illumination striking the active area of the micromirror array. Under this framework, the process of designing the partitioning geometry that determines optical functionality involves making iterative manipulations to an amplitude mask matrix representing the micromirror array. This matrix is first constructed as a binary 2D image of all potential micromirror pixels that

may be placed in the active region of interest in accordance with the tiling scheme defined by the pixel-level design process and at a resolution (i.e. matrix element size) that is comparable to the wavelength of interest ($\approx 1\ \mu m$). A segmentation function returning the set of all 8-connected objects in a binary image is subsequently employed to expand the original image into separate matrices of identical size isolating each micromirror pixel. Each of these pixels may then be kept or removed from the active area via simple matrix addition/subtraction operations. Additionally, object dilation and erosion operations may be used to adjust pixel fill factor, and pixel grouping indicative of co-wiring and joint actuation is performed by adding distinct single-pixel matrices together. Once a pixel partitioning iteration culminates in a finite number n of matrices, each corresponding to an independently addressable actuation channel, mirror efficiency can be accounted for by scaling these matrices, and therefore the unit amplitudes denoting active pixel regions, with the experimentally measured reflectance of the chosen pixel mirror surface at the wavelength of interest. Background array reflectivity may also be incorporated into the framework by constructing a separate static matrix with a non-zero complex amplitude across non-mirror regions and with null amplitudes in all active mirror regions. Lastly, in order to simulate optical performance for a given phase mask produced by the array, active single-channel matrices are multiplied by their respective exponential phase factors and summed together along with the static background reflection matrix. The resulting complex matrix is then subjected to a 2D fast Fourier transform (FFT) operation and scaled in accordance with Parseval's theorem to obtain the complex amplitude profile at the rear focal plane of the lens (the matrix's unit element dimensions are also scaled by a factor λf). Fresnel propagation may then be employed to obtain the complex amplitude profile of any plane that is both parallel and proximal to the rear focal plane: this feature is implemented via pre-multiplication by a Fresnel propagation kernel prior to the FFT operation in order to avoid the computational burden of an additional convolution operation in the framework.

To further illustrate the developed array-scale framework along with its capacity to assess

process variation impacts, we present in this work a full design iteration targeting axial focusing as shown in Figure 4.2. Given that axial focusing requires only radial phase control in order to produce spherical phase profiles at the micromirror plane, we have simplified the design process by pre-partitioning array pixels into 45 elemental rings of identical track width. Since the ADI AD5535B DAC chosen to drive the array has a total of 32 independent channels, designing the axial focusing array becomes a matter of finding the optimal regrouping scheme that consolidates these 45 elemental rings into the 32 rings that determine the final pixel partitioning geometry. The quality of a given partitioning geometry is evaluated by examining focusing performance, as measured by peak optical intensity profile across the full depth range of the output volume, for several phase masks targeting different depths. For a certain target depth at a signed distance d_z from the rear focal plane of the offset lens, the phase shift $\Delta\phi$ required at an array ring bounded by radii a and b ($a < b$) is given by:

$$\Delta\phi = \frac{1}{b-a}\int_a^b \frac{2\,\pi\,f^2}{d_z\,\lambda}\left(1-\sqrt{1-\frac{(d_z\,r)^2}{f^4}}\right)d\,r + \phi$$

where ϕ is some global phase offset applied uniformly to all rings.

Similarly, in the case of 1D beamsteering along a certain axis x at the rear focal plane, for a target lateral deflection to a signed distance d_x from the optical axis, the phase shift $\Delta\phi$ required at an array band bounded by coordinates e and f ($e < f$) along the relevant cartesian axis would be given by:

$$\Delta\phi = \frac{1}{f-e}\int_e^f -2\,\pi\frac{d_x}{\lambda\,f}\,x\,dx + \phi = -\pi\frac{d_x}{\lambda\,f}\,(e+f) + \phi$$

Importantly, one of the most useful features of the described array-scale framework is its ability to incorporate the impact of process variations into simulated performance based on *a priori* experimentally-obtained distribution data for the chosen pixel structures. This

is achieved in a Monte Carlo-based approach where deviations to phase values across the array are introduced by generating random numbers using measured distribution parameters, namely standard deviation (assuming normality for simplicity). Once this process has been repeatedly performed in order to construct several non-ideal phase profiles that are representative of what may be produced by actual fabricated arrays for a given target depth, computational simulations of optical propagation through the system are performed to obtain mean optical performance and expected deviation ranges.

We note that, for the fabricated pixel structures, actuation-dependent displacement deviations that vary with applied phase dominate over static variations, as illustrated in Figure 4.2 by the fact that rings imparting greater phase shifts are subject to greater phase heterogeneity. Given such behavior, modulating the global phase offset parameter ϕ to minimize mean actuation across all channels can be useful in improving focusing performance for a given target depth. In addition, as part of this same phase modulation process, applied phases may be constrained to a finite set of discrete values in order to account for driver quantization. While the ADI AD5535B DACs used in this work are capable of 14-bit drive and thus a millivolt-scale precision that is eclipsed by the actuation-dependent variation exhibited by the employed pixel structures, other design iterations may be constrained by driving schemes of lower bit-depth and therefore significant quantization effects.

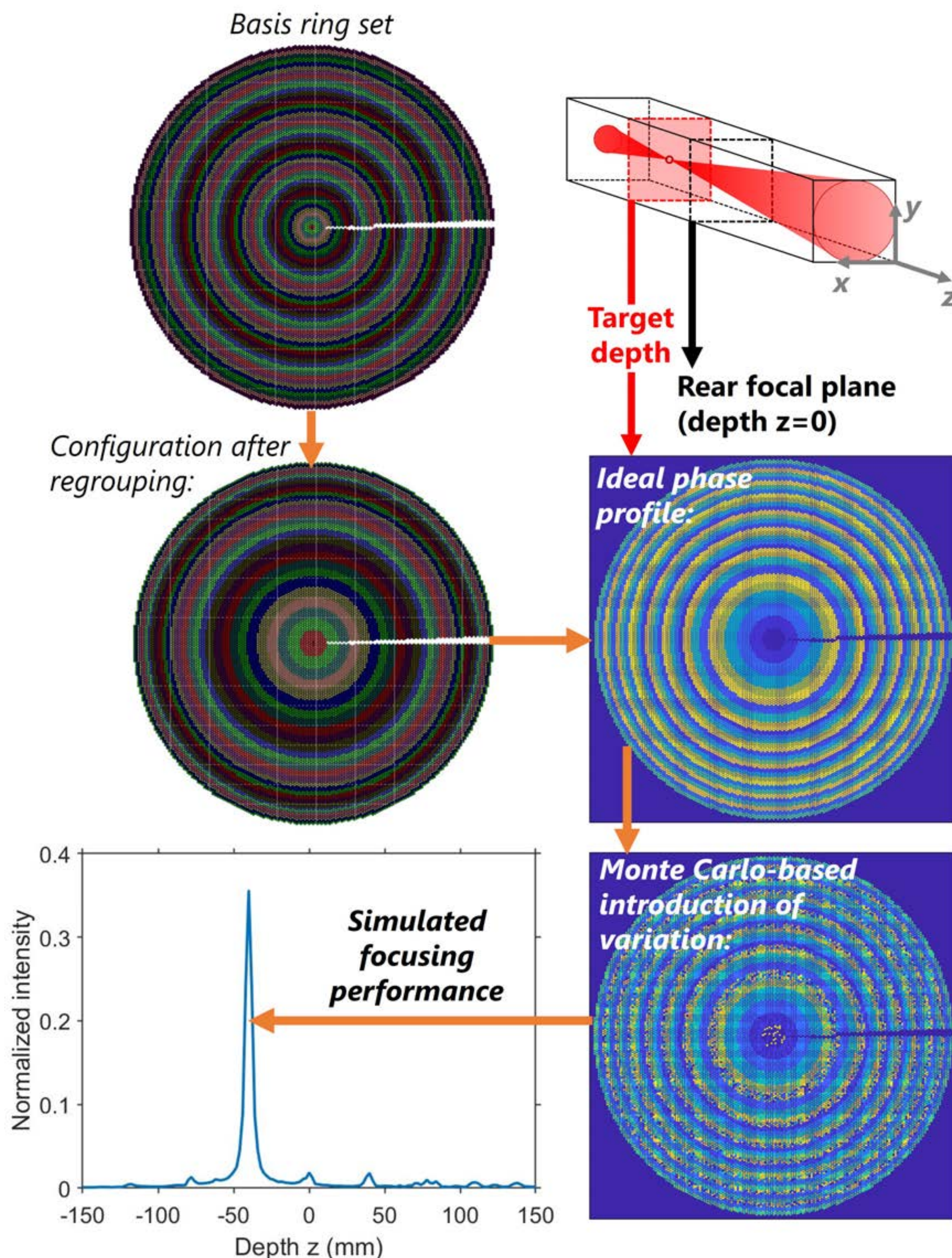

Figure 4.2: Simulation pipeline for axial focusing array. Using a layout of the fabricated array obtained by regrouping a basis set of elemental rings, ideal phase masks are first generated for each target focus depth. Variations to these ideal phase masks can subsequently be repeatedly introduced to computationally reproduce non-idealities in optical performance due to mismatches in pixel behavior and topography. Lastly, mean optical performance (on-axis intensity across depth z) can be obtained from propagation simulations.

4.3 Simulated performance results

In the case of axial focusing, we find that the most optimal partitioning geometry results in rings of decreasing track width away for the center of the array as shown in Figure 8 because spherical phase profiles exhibit increasing gradients with increasing radius. Such a geometry would, for instance, differ from the optimal partitioning scheme for Bessel beam shaping, which also requires radial phase control but involves conical phase profiles with gradients of uniform magnitude instead of spherical profiles, resulting in rings of identical track width. Simulation results for the finalized partitioning geometry are shown in Figure 4.3. Operating range across depth z is defined as the range across which the on-axis peak intensity of the scanned spot is greater than that of other peaks resulting from higher-order diffraction effects. The full width at half maximum ($FWHM_{x,y,z}$) of the scanned spot was used as a measure of spot size. Spot intensity drops as target depth increases in either direction because escalating defocus requires sharper radial phase gradients and, in discrete array systems such as ones with micromirrors, efficiency scales inversely with phase gradient under a $sinc^2$ relationship [52]. We find that the dynamic dioptric power range of the 8.2 mm diameter array alone (excluding the contribution of the offset lens) is ± 2.89 $diopters$, which is comparable the ranges of commercially available optofluidic lenses that also make use of offset lenses [53]. In addition, as shown in Figure 4.3(b), lateral spot dimensions do not deviate significantly from the diffraction-limited spot size set by the aperture, focal length and wavelength of the optical system. However, the introduction of process variations reveals the existence of an asymmetry in focusing performance for target depths on either side of the rear focal plane. Specifically, the discontinuity seen around $x = 0$ in Figure 4.3(b) is due to the transition from a shallow convex mirror profile with minor pixel actuation around the central array region to a shallow concave mirror profile with extensive actuation around the same central array region. Since variation in pixel behavior increases with the extent of actuation, concave mirror profiles thus exhibit a slight decrease in focusing performance

compared to convex profiles. This trend is also reflected in Figure 4.3(a), where concave mirror profiles exhibit reduced efficiencies compared to their convex-shaped counterparts.

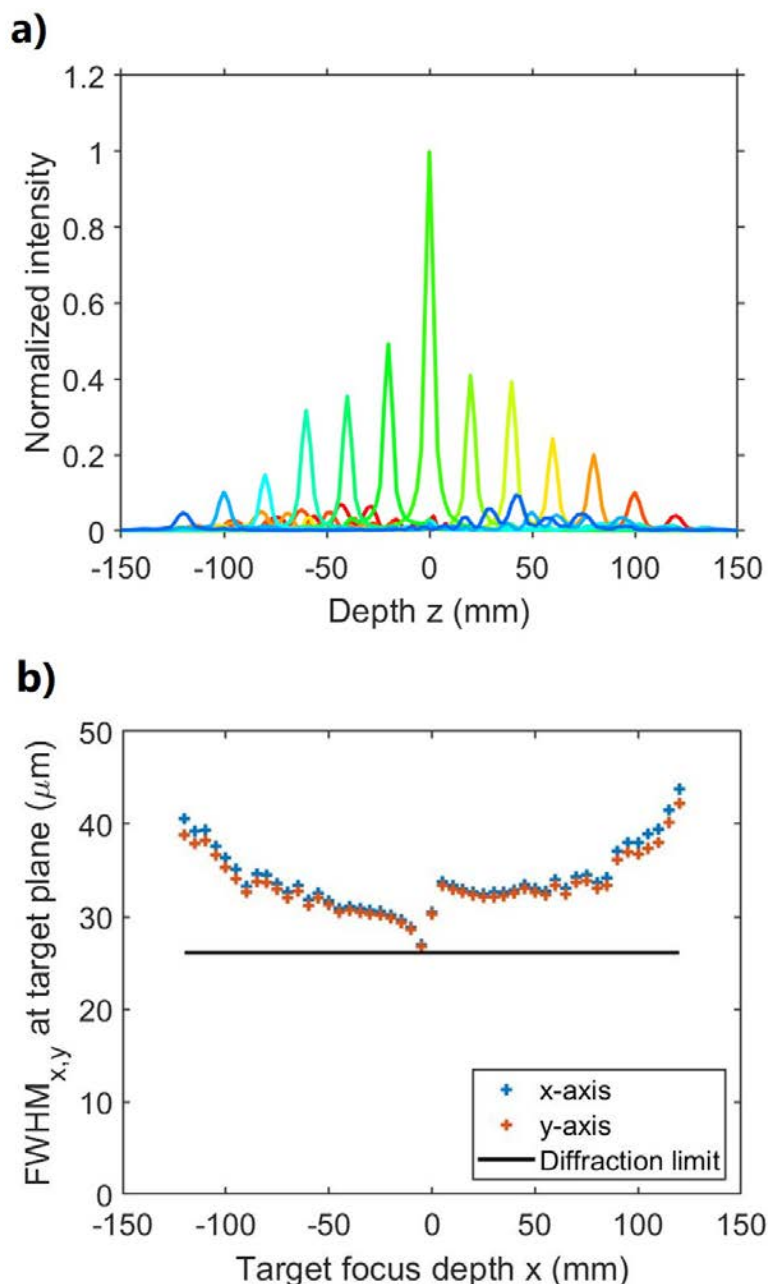

Figure 4.3: Full simulation results for designed axial focusing array using a 1040 nm Gaussian beam for illumination and a 200 mm focal length offset lens. a) On-axis normalized intensity profile for array phase masks across the entire operating range. b) Lateral dimensions, specifically full widths at half maximum ($FWHM$) along x and y axes, of focused spots at their target depths across the operating range. Black line corresponds to the $FWHM$ of a diffraction-limited spot at $z = 0$ for the given array aperture and lens focal length.

5. Discussion and conclusions

Overall, the described pixel-scale and array-scale computational frameworks offer a modular, systematic and efficient path for both *de novo* design iterations and adaptive reconfigurations of pixel-based primitive spatial light modulation tools. At the core of our development approach is an iterative pixel partitioning process for grouped pixel drive that offers two advantages: an alleviation of operating burden via tailored consolidation of drive channels, and a pixel averaging effect that rescues optical functionality in the face of significant spatial process variation. Through a development process interweaving simulation-based design and experimental characterization, we also demonstrate that both viable pixel-level structures and competitive array-scale optical modulation tools (such as ones for axial focusing) can feasibly be constructed from standard, widely accessible fabrication processes with off-the-shelf drivers boasting channel counts on the order of $\approx 10^1$. The proposed development approach to optical modulation tools also has bearings on the design of complex optical manipulation systems involving multiple tools: the allotment of required DoF can indeed be re-envisioned to allow for more compact driving schemes under cascaded operation. For instance, by recognizing that axial defocusing can be achieved by cascading cylindrical focusing along two orthogonal directions, a 3D scanning system may be constructed with two identical ribbon-partitioned arrays (one array for X-axis steering and cylindrical focusing, followed by another array rotated by 90° for Y-axis steering and cylindrical focusing) instead of three arrays (one for X-axis steering, a second for Y-axis steering, and a third for axial focusing) [4]. Thus, with such system-level considerations, complex light manipulation systems can be assembled from a minimal number of primitive optical modulation tools for even greater reductions in total number of drive channels.

A number of insights and potential improvements can be gleaned from the design iteration

endeavored in this work. First, the use of pixelated, spatially discrete phased arrays as active areas instead of continuous phase surfaces alters efficiency behavior. Peak efficiency for a given array becomes set not only by the reflectivity of the mirror surface, but also by the square of the array's pixel fill factor. Efficiency then drops off from this maximum value in a $sinc^2$ fashion as phase gradient increases, i.e. as the extent of optical modulation/deflection increases. The altered behavior must be accounted for with performance margins in both pixel-level and array-level designs across applications that impose uniformity or threshold constraints on efficiency. Second, since the proposed tools rely on co-wired pixel operation, it is imperative that a single-pixel failure event such as electrode shorting does not result in whole-channel failure. Accordingly, fail-safe mechanisms such as gap stop structures and insulating barriers are crucial to the pixel-level design process: once isolated properly, a single-pixel failure typically results in negligible degradation to array-scale performance due to pixel averaging. Third, power handling, which is a critical aspect of desired performance in some applications including laser micro-machining [54], was not addressed in the reported design iteration and experimental characterization. A survey of the literature reveals that micromirrors are susceptible to reflectance losses due to eutectic bond widening as well as mirror delamination due to gaseous release at the temperatures experienced under high optical powers [46]. While an extrapolation of previously reported optical power limits measured across PolyMUMPS micromirrors suggests that our designed arrays should be able to withstand over 10 W without sustaining permanent damage [46], opto-thermal analyses and characterizations would be required as part of this design process for an accurate assessment of power handling.

We identify a number of future opportunities that can expand the features and capabilities of both the described framework and the resulting array-based tools. While the framework's current embodiment models process variations as being normally distributed and uncorrelated noise-like phase fluctuations, improved simulation results and design processes may be obtained by modeling these variations more accurately as location-dependent phase

deviations given that the underlying parameters driving these non-uniformities in pixel performance, namely layer thicknesses and residual stress levels, exhibit regional continuity. Though such an approach entails more comprehensive characterizations of process variation post-fabrication, it also offers a path to enhanced optical performance via regional partitioning schemes that allow for channel-specific calibration and correction. Moreover, fabricated tools may be outfitted with limited dynamic runtime rewiring capabilities through the placement of active electrical routing structures composed of electromechanical relays (akin to cross-connect architectures) outside of the array region for multi-mode operation using the same number of driving channels [55]. Finally, for applications that exhibit temporal integration and averaging such as AR/VR [12], global phase offsets may be modulated across several frames to improve optical performance by washing out artifacts resulting from unwanted diffraction effects or actuation-dependent process variations.

References

[1] N. T. Ersumo, C. Yalcin, N. Antipa, N. Pegard, L. Waller, D. Lopez, and R. Muller, "Design framework for high-speed 3d scanning tools and development of an axial focusing micromirror-based array," *MOEMS and Miniaturized Systems XIX, SPIE Opto*, 2020.

[2] T. W. Clark, R. F. Offer, S. Franke-Arnold, A. S. Arnold, and N. Radwell, "Comparison of beam generation techniques using a phase only spatial light modulator," *Optics express*, vol. 24, no. 6, pp. 6249–6264, 2016, ISSN: 1094-4087.

[3] Z. Zhang, Z. You, and D. Chu, "Fundamentals of phase-only liquid crystal on silicon (lcos) devices," *Light: Science & Applications*, vol. 3, no. 10, e213–e213, Oct. 24, 2014, ISSN: 2047-7538. DOI: 10.1038/lsa.2014.94.

[4] J. R. Landry, S. S. Hamann, and O. Solgaard, "Random access cylindrical lensing and beam steering using a high-speed linear phased array," *IEEE Photonics Technology Letters*, vol. 32, no. 14, pp. 859–862, 2020, ISSN: 1041-1135.

[5] P. S. Salter and M. J. Booth, "Adaptive optics in laser processing," *Light: Science & Applications*, vol. 8, no. 1, pp. 1–16, 2019, ISSN: 2047-7538.

[6] C. Rodríguez, Y. Liang, R. Lu, and N. Ji, "Three-photon fluorescence microscopy with an axially elongated bessel focus," *Optics letters*, vol. 43, no. 8, pp. 1914–1917, 2018, ISSN: 1539-4794.

[7] S.-W. Cho, H. Kim, J. Hahn, and B. Lee, "Generation of multiple vortex-cones by direct-phase modulation of annular aperture array," *Applied Optics*, vol. 51, no. 30, pp. 7295–7302, 2012, ISSN: 2155-3165.

[8] S. A. Matthews, M. Collados, M. Mathioudakis, and R. Erdelyi, "The european solar telescope (est)," *Ground-based and Airborne Instrumentation for Astronomy VI*, vol. 9908, p. 990 809, 2016.

[9] V. Emiliani, A. E. Cohen, K. Deisseroth, and M. Häusser, "All-optical interrogation of neural circuits.," *The Journal of neuroscience : the official journal of the Society for Neuroscience*, vol. 35, no. 41, pp. 13 917–26, Oct. 14, 2015, ISSN: 1529-2401. DOI: 10.1523/JNEUROSCI.2916-15.2015.

[10] Y. Liang, Y. Cai, Z. Wang, M. Lei, Z. Cao, Y. Wang, M. Li, S. Yan, P. R. Bianco, and B. Yao, "Aberration correction in holographic optical tweezers using a high-order optical vortex," *Applied optics*, vol. 57, no. 13, pp. 3618–3623, 2018, ISSN: 2155-3165.

[11] Y. Zhang, S. Poonja, and A. Roorda, "Mems-based adaptive optics scanning laser ophthalmoscopy," *Optics letters*, vol. 31, no. 9, pp. 1268–1270, 2006, ISSN: 1539-4794.

[12] D. Dunn, C. Tippets, K. Torell, P. Kellnhofer, K. Akşit, P. Didyk, K. Myszkowski, D. Luebke, and H. Fuchs, "Wide field of view varifocal near-eye display using see-through deformable membrane mirrors," *IEEE transactions on visualization and computer graphics*, vol. 23, no. 4, pp. 1322–1331, 2017, ISSN: 1077-2626.

[13] M. Žurauskas, O. Barnstedt, M. Frade-Rodriguez, S. Waddell, and M. J. Booth, "Rapid adaptive remote focusing microscope for sensing of volumetric neural activity," *Biomedical Optics Express*, vol. 8, no. 10, p. 4369, Oct. 1, 2017, ISSN: 2156-7085. DOI: 10.1364/BOE.8.004369.

[14] J. Hasselbach, S. Bogatscher, and C. Rembe, "Laser scanning module with large sending aperture and inherent high angular position accuracy for 3d lidar," *Optical Sensors 2019*, vol. 11028, p. 1 102 804, 2019.

[15] S.-B. Wen, A. Bhaskar, and H. Zhang, "Scanning digital lithography providing high speed large area patterning with diffraction limited sub-micron resolution," *Journal of Micromechanics and Microengineering*, vol. 28, no. 7, p. 75 011, 2018, ISSN: 0960-1317.

[16] K. J. Dowling, B. A. Bhut, M. S. Lucas, S. Sivam, Y. J. Hsu, A. Shahar, and J. Li, "Position observer based galvanometer scanner and xy stage synchronization for large area processing," *Laser Applications in Microelectronic and Optoelectronic Manufacturing (LAMOM) XXV*, vol. 11267, p. 1 126 713, 2020.

[17] G. Römera and P. Bechtoldb, "Electro-optic and acousto-optic laser beam scanners-invited paper," *Physics procedia*, vol. 56, pp. 29–39, 2014.

[18] M. Bathe-Peters, P. Annibale, and M. J. Lohse, "All-optical microscope autofocus based on an electrically tunable lens and a totally internally reflected ir laser," *Optics express*, vol. 26, no. 3, pp. 2359–2368, 2018, ISSN: 1094-4087.

[19] Y. Shao, D. L. Dickensheets, and P. Himmer, "3-d moems mirror for laser beam pointing and focus control," *IEEE Journal of Selected Topics in Quantum Electronics*, vol. 10, no. 3, pp. 528–535, 2004, ISSN: 1077-260X.

[20] P. Janin, R. Bauer, P. Griffin, E. Riis, and D. Uttamchandani, "Characterization of a fast piezoelectric varifocal mems mirror," *2018 International Conference on Optical MEMS and Nanophotonics (OMN)*, pp. 1–5, Jul. 2018. DOI: 10.1109/OMN.2018.8454626.

[21] B. N. Ozbay, J. T. Losacco, R. Cormack, R. Weir, V. M. Bright, J. T. Gopinath, D. Restrepo, and E. A. Gibson, "Miniaturized fiber-coupled confocal fluorescence microscope with an electrowetting variable focus lens using no moving parts," *Optics letters*, vol. 40, no. 11, pp. 2553–2556, 2015, ISSN: 1539-4794.

[22] L. Wang, T. Hayakawa, and M. Ishikawa, "Dielectric-elastomer-based fabrication method for varifocal microlens array," *Optics express*, vol. 25, no. 25, pp. 31 708–31 717, 2017, ISSN: 1094-4087.

[23] Y.-J. Wang, H.-A. Hsieh, and Y.-H. Lin, "Electrically tunable gradient-index lenses via nematic liquid crystals with a method of spatially extended phase distribution," *Optics express*, vol. 27, no. 22, pp. 32 398–32 408, 2019, ISSN: 1094-4087.

[24] C. B. Arnold, C. Theriault, D. Amrhein, S. Kang, and E. Dotsenko, "Ultra-high-speed variable focus optics for novel applications in advanced imaging," *Photonic Instrumentation Engineering V*, vol. 10539, Y. G. Soskind, Ed., p. 1, Feb. 22, 2018. DOI: 10.1117/12.2294487.

[25] J. Heberle, P. Bechtold, J. Strauß, and M. Schmidt, "Electro-optic and acousto-optic laser beam scanners," *Laser-based Micro- and Nanoprocessing X*, vol. 9736, U. Klotzbach, K. Washio, and C. B. Arnold, Eds., p. 97360L, Mar. 4, 2016. DOI: 10.1117/12.2212208.

[26] K. Mishra, D. van den Ende, F. Mugele, K. Mishra, D. Van den Ende, and F. Mugele, "Recent developments in optofluidic lens technology," *Micromachines*, vol. 7, no. 6, p. 102, Jun. 10, 2016, ISSN: 2072-666X. DOI: 10.3390/mi7060102.

[27] H.-C. Lin, M.-S. Chen, and Y.-H. Lin, "A review of electrically tunable focusing liquid crystal lenses," *Transactions on Electrical and Electronic Materials*, vol. 12, no. 6, pp. 234–240, Dec. 25, 2011, ISSN: 1229-7607. DOI: 10.4313/TEEM.2011.12.6.234.

[28] P.-Y. Madec, "Overview of deformable mirror technologies for adaptive optics and astronomy," *Adaptive Optics Systems III*, vol. 8447, B. L. Ellerbroek, E. Marchetti, and J.-P. Véran, Eds., pp. 844 705–844705-18, Sep. 13, 2012. DOI: 10.1117/12.924892.

[29] G. D. Reddy and P. Saggau, "Fast three-dimensional laser scanning scheme using acousto-optic deflectors," *Journal of Biomedical Optics*, vol. 10, no. 6, p. 064 038, 2005, ISSN: 10833668. DOI: 10.1117/1.2141504.

[30] D. M. Benton, "Multiple beam steering using dynamic zone plates on a micromirror array," *Optical Engineering*, vol. 57, no. 07, p. 1, Jul. 27, 2018, ISSN: 0091-3286. DOI: 10.1117/1.OE.57.7.073109.

[31] A. M. Scott, K. D. Ridley, D. C. Jones, M. E. McNie, G. W. Smith, K. M. Brunson, A. Lewin, and K. L. Lewis, "Retro-reflective communications over a kilometre range using

a mems-based optical tag," *Unmanned/Unattended Sensors and Sensor Networks VI*, vol. 7480, p. 74800L, 2009.

[32] Y. Wang, G. Zhou, X. Zhang, K. Kwon, P.-A. Blanche, N. Triesault, K.-s. Yu, and M. C. Wu, "2d broadband beamsteering with large-scale mems optical phased array," *Optica*, vol. 6, no. 5, pp. 557–562, 2019, ISSN: 2334-2536.

[33] Y. Song, R. M. Panas, and J. B. Hopkins, "A review of micromirror arrays," *Precision Engineering*, vol. 51, pp. 729–761, Jan. 1, 2018, ISSN: 0141-6359. DOI: 10.1016/J.PRECISIONENG.2017.08.012.

[34] A. Kumar, D. Bansal, P. Kumar, and K. Rangra, "Post-release deformation and curvature correction of an electrothermally actuated mems bilayer platform," *Microelectronic Engineering*, vol. 221, p. 111 192, 2020, ISSN: 0167-9317.

[35] Y. Yan, X. Tian, R. Liang, and J. Sasian, "Optical performance evaluation and chromatic aberration correction of a focus tunable lens used for 3d microscopy," *Biomedical Optics Express*, vol. 10, no. 12, pp. 6029–6042, 2019, ISSN: 2156-7085.

[36] A. Martínez, M. del Mar Sánchez-López, and I. Moreno, "Phasor analysis of binary diffraction gratings with different fill factors," *European Journal of Physics*, vol. 28, no. 5, p. 805, 2007, ISSN: 0143-0807.

[37] B. Borghuis, D. Tadin, M. Lankheet, J. Lappin, and W. van de Grind, "Temporal limits of visual motion processing: Psychophysics and neurophysiology," *Vision*, vol. 3, no. 1, p. 5, Jan. 26, 2019, ISSN: 2411-5150. DOI: 10.3390/vision3010005.

[38] A. Gehner, S. Döring, D. Rudloff, D. Kunze, P. Dürr, S. Francés, L. Hänsel, H. Torlee, A. Elgner, and M. Eckert, "Novel cmos-integrated 512x320 tip-tilt micro mirror array and related technology platform," *MOEMS and Miniaturized Systems XIX*, vol. 11293, p. 1 129 302, 2020.

[39] M. Lapisa, F. Zimmer, F. Niklaus, A. Gehner, and G. Stemme, "Cmos-integrable piston-type micro-mirror array for adaptive optics made of mono-crystalline silicon using 3-d integration," *Micro Electro Mechanical Systems, 2009. MEMS 2009. IEEE 22nd International Conference on*, pp. 1007–1010, Jan. 2009. DOI: 10.1109/MEMSYS.2009.4805556.

[40] G. P. Watson, V. Aksyuk, M. E. Simon, D. M. Tennant, R. A. Cirelli, W. M. Mansfield, F. Pardo, D. O. Lopez, C. A. Bolle, A. R. Papazian, N. Basavanhally, J. Lee, R. Fullowan, F. Klemens, J. Miner, A. Kornblit, T. Sorsch, L. Fetter, M. Peabody, J. E. Bower, J. S. Weiner, and Y. L. Low, "Spatial light modulator for maskless optical projection lithography," *Journal of Vacuum Science & Technology B: Microelectronics and Nanometer Structures Processing, Measurement, and Phenomena*, vol. 24, no. 6, pp. 2852–2856, Nov. 30, 2006, ISSN: 1071-1023. DOI: 10.1116/1.2387156.

[41] P. J. Ryan, S. A. Cornelissen, V. C. Lam, and P. A. Bierden, "Performance analysis of two high actuator count mems deformable mirrors," *MEMS Adaptive Optics VII*, vol. 8617, p. 861 705, 2013.

[42] T. Wang, C. Wu, D. G. Ouzounov, W. Gu, F. Xia, M. Kim, X. Yang, M. R. Warden, and C. Xu, "Quantitative analysis of 1300-nm three-photon calcium imaging in the mouse brain," *Elife*, vol. 9, e53205, 2020, ISSN: 2050-084X.

[43] E.-S. Kim, Y.-H. Cho, and M.-U. Kim, "Effect of holes and edges on the squeeze film damping of perforated micromechanical structures," *Micro Electro Mechanical Systems, 1999. MEMS'99. Twelfth IEEE International Conference on*, pp. 296–301, 1999.

[44] W. C. Young, R. G. Budynas, A. M. Sadegh, *et al.*, *Roark's formulas for stress and strain*. McGraw-Hill New York, 2002, vol. 7.

[45] A. Cowen, B. Hardy, R. Mahadevan, S. W. .-. M. Inc, U. 2011, J. Carter, A. Cowen, B. Hardy, R. M. .-. M. I. . . ., and U. 2005, "Polymumps design handbook," *MEMSCAP*, 2005.

[46] D. M. Burns and V. M. Bright, "Optical power induced damage to microelectromechanical mirrors," *Sensors and Actuators A: Physical*, vol. 70, no. 1-2, pp. 6–14, Oct. 1998, ISSN: 09244247. DOI: 10.1016/S0924-4247(98)00106-X.

[47] F. B. Dejene and R. O. Ocaya, "Electrical, optical and structural properties of pure and gold-coated vo2 thin films on quartz substrate," *Current Applied Physics*, vol. 10, no. 2, pp. 508–512, 2010, ISSN: 1567-1739.

[48] J. B. Hopkins, R. M. Panas, Y. Song, and C. D. White, "A high-speed large-range tip-tilt-piston micromirror array," *Journal of Microelectromechanical Systems*, vol. 26, no. 1, pp. 196–205, 2016, ISSN: 1057-7157.

[49] E. Arbabi, A. Arbabi, S. M. Kamali, Y. Horie, M. Faraji-Dana, and A. Faraon, "Mems-tunable dielectric metasurface lens," *Nature Communications*, vol. 9, no. 1, p. 812, Dec. 23, 2018, ISSN: 2041-1723. DOI: 10.1038/s41467-018-03155-6.

[50] I. W. Jung, S. Kim, and O. Solgaard, "High-reflectivity broadband photonic crystal mirror mems scanner with low dependence on incident angle and polarization," *Journal of microelectromechanical systems*, vol. 18, no. 4, pp. 924–932, 2009, ISSN: 1057-7157.

[51] F. Montfort, Y. Emery, F. Marquet, E. Cuche, N. Aspert, E. Solanas, A. Mehdaoui, A. Ionescu, and C. Depeursinge, "Process engineering and failure analysis of mems and moems by digital holography microscopy (dhm)," *Reliability, Packaging, Testing, and Characterization of MEMS/MOEMS VI*, vol. 6463, 64630G, 2007.

[52] J. C. Shane, D. J. McKnight, A. Hill, K. Taberski, and S. Serati, "Designing a new spatial light modulator for holographic photostimulation," *Optical Trapping and Optical Micromanipulation XVI*, vol. 11083, K. Dholakia and G. C. Spalding, Eds., p. 3, Sep. 9, 2019. DOI: 10.1117/12.2528558.

[53] A. R. Aramendía, I. Grulkowski, A. J. Villar, S. Manzanera, Y. Chen, J. Mompean, F. Díaz-Doutón, J. Pujol, J. L. Güell, and P. Artal, "Optimization of a ss-oct with a focus tunable lens for enhanced visualization of ocular opacities," *Optical Coherence Tomography and Coherence Domain Optical Methods in Biomedicine XXIII*, vol. 10867, 108673E, 2019.

[54] T.-H. Chen, R. Fardel, and C. B. Arnold, "Ultrafast z-scanning for high-efficiency laser micro-machining," *Light: Science & Applications*, vol. 7, no. 4, p. 17181, Apr. 20, 2018, ISSN: 2047-7538. DOI: 10.1038/lsa.2017.181.

[55] D. Dubuc, K. Grenier, and J. Iannacci, "Rf-mems for smart communication systems and future 5g applications," in *Smart Sensors and MEMs*, Elsevier, 2018, pp. 499–539.